Beamspace MIMO for Millimeter-Wave Communications: System Architecture, Modeling, Analysis, and Measurements

John Brady, *Student Member, IEEE,* Nader Behdad, *Member, IEEE,* and Akbar Sayeed, *Fellow, IEEE*

***Abstract*—Millimeter-wave wireless systems are emerging as a promising technology for meeting the exploding capacity requirements of wireless communication networks. Besides large bandwidths, small wavelengths at mm-wave lead to a high dimensional spatial signal space, that can be exploited for significant capacity gains through high dimensional multiple-input multiple-output (MIMO) techniques. In conventional MIMO approaches, optimal performance requires prohibitively high transceiver complexity. By combining the concept of beamspace MIMO communication with a hybrid analog-digital transceiver, Continuous Aperture Phased (CAP) MIMO achieves near-optimal performance with dramatically lower complexity. This paper presents a framework for physically-accurate computational modeling and analysis of CAP-MIMO, and reports measurement results on a DLA-based prototype for multi-mode line-of-sight communication. The model, based on a critically sampled system representation, is used to demonstrate the performance gains of CAP-MIMO over state-of-the-art designs at mm-wave. For example, a CAP-MIMO system can achieve a spectral efficiency of 10-20 bits/s/Hz with a 17-31dB power advantage over state-of-the-art, corresponding to a data rate of 10-200 Gbps with 1-10GHz system bandwidth. The model is refined to analyze critical sources of power loss in an actual multi-mode system. The prototype-based measurement results closely follow the theoretical predictions, validating CAP-MIMO theory, and illustrating the utility of the model.**

***Index Terms*—Analog beamforming, Discrete lens array, Gigabit wireless, High dimensional MIMO, Lens Antennas, Millimeter-wave communication, MIMO systems, Transceiver complexity**

I. Introduction

The rapid proliferation of consumer wireless devices is creating a spectrum crisis at the current wireless frequencies. A variety of communication and signal processing techniques are currently being pursued for interference management and efficient use of the available spectrum, including cognitive radio and multi-antenna technology. Despite these efforts, there is a growing consensus that meeting the dramatically increasing data demands of wireless devices and applications will require transformative new technologies and methodologies. While they have been under research for several years [1], driven by advances in enabling technology, millimeter-wave (mm-wave) wireless systems, operating from 30-300GHz, are emerging as a promising technology for meeting the exploding bandwidth requirements by enabling multi-Gbps speeds [2].

The authors are with the Department of Electrical and Computer Engineering, University of Wisconsin-Madison, Madison, WI 53706 USA

This work is supported in part by the National Science Foundation under Grant ECCS-1052628, and the Wisconsin Alumni Research Foundation (WARF).

Mm-wave systems offer unique opportunities for enabling high data rate wireless communication. First, moving to the mm-wave regime opens up large portions of unused spectrum that can support orders of magnitude larger bandwidths (10s of GHz) compared to existing systems. Second, exploiting the spatial dimension is particularly promising: for a given antenna size A the small wavelength, λ, leads to a dramatic increase in the dimension of the spatial signal space, $n = \frac{4A}{\lambda^2}$. In addition to creating narrow, high-gain beams, the high-dimensional spatial signal space can be exploited by multiple-input multiple-output (MIMO) transceivers for significant improvement in spectral efficiency through spatial multiplexing of simultaneous data streams. Due to the highly directional nature of propagation, line-of-sight (LoS) propagation plays an important role at mm-wave. While the spatial multiplexing advantages of MIMO have traditionally rested on multipath propagation [3]–[5], mm-wave systems can exploit MIMO operation even in LoS propagation for both point-to-point (P2P) and point-to-multipoint (P2MP) network links.

While the dimension of the spatial signal space, n, can be quite high ($10^3 - 10^5$), due to the highly directional propagation, the actual number of spatial communication modes, p, is much smaller: $p \ll n$. However, current state-of-the-art mm-wave systems fail to take full advantage of the spatial dimension. "Dish" systems with continuous aperture antennas, such as the commercial systems offered by Siklu (http://www.siklu.com/) and LightPointe (http://www.lightpointe.com/) for mm-wave wireless backhaul, exploit narrow, high gain beams, but only support a single data stream ($p = 1$). Conventional MIMO systems with widely spaced discrete antennas (due to complexity considerations) [6]–[8] support spatial multiplexing ($p > 1$), but suffer from reduced gain and compromised security due to grating lobes. In conventional MIMO designs, full exploitation of the spatial dimension requires critically (half-wavelength) spaced antenna arrays, but this approach suffers from a prohibitively high transceiver complexity on the order of n.

The recently proposed Continuous Aperture Phased MIMO (CAP-MIMO) transceiver architecture [9], [10] is based on the concept of beamspace MIMO communication [5] to enable efficient access to the p communication modes of an n-dimensional mm-wave link. CAP-MIMO uses a hybrid analog-digital front-end in which a high-resolution discrete lens array (DLA) is used for *analog* spatial beamforming. The DLA-based front-end enables CAP-MIMO to achieve near-optimal performance with dramatically lower transceiver complexity,

on the order of p, compared to the order n complexity of conventional MIMO. Furthermore, initial theoretical results show that CAP-MIMO can potentially deliver very compelling performance gains over the state-of-the-art in terms of power efficiency, capacity, and operational capability.

This paper builds on the theoretical foundations of CAP-MIMO in [9], [10], overviewed in Sec. II, to investigate the modeling, design, and analysis of a physically realizable CAP-MIMO system. There are three main contributions reported in this paper. First, we outline a general framework for accurate computational modeling of the CAP-MIMO system in Sec. III, including modeling of the DLA, channel, and overall system. Second, the computational framework is used to analyze the performance of a CAP-MIMO system in Sec. IV. In Sec. V, we present promising measurement results based on a DLA-based prototype system to validate and refine the basic CAP-MIMO theory and the modeling framework. Sec. VI presents a discussion of results and concluding remarks.

Notation: Lowercase boldfaced letters (e.g., $\mathbf{h}$) denote complex-valued column vectors, and uppercase boldfaced letters denote matrices (e.g, $\mathbf{H}$). Elements of vectors or matrices are not boldfaced; e.g, $h(\ell)$ and $H(\ell, m)$. $\mathrm{tr}(\mathbf{H})$ denotes the trace, $\det(\mathbf{H})$ the determinant, $\mathbf{H}^T$ the transpose, and $\mathbf{H}^H = (\mathbf{H}^T)^*$ the complex conjugate transpose of $\mathbf{H}$. The notation $\mathbf{x} \sim \mathcal{CN}(\mathbf{m}, \mathbf{\Sigma})$ denotes a complex Gaussian vector $\mathbf{x}$ with mean $\mathbf{m} = E[\mathbf{x}]$ and covariance matrix $\mathbf{\Sigma} = E[(\mathbf{x}-\mathbf{m})(\mathbf{x}-\mathbf{m})^H]$, where $E[\cdot]$ denotes the statistical expectation operator. We will use the terms modes and beams interchangeably.

II. CAP MIMO Overview

CAP-MIMO theory is based on a finite-dimensional system representation induced by critical sampling of the antenna apertures. This provides a complex baseband system model that serves as the foundation for theoretical, computational, and experimental design and analysis. Consider a link consisting of a 1D linear transmit antenna of length L_T and a 1D linear receive antenna of length L_R separated by a link length of $R \gg L_T, L_R$ operating at carrier frequency f_c, with wavelength λ. Critical sampling results in signal space dimensions n_T and n_R, where

$$n_{1D} = \frac{2L}{\lambda}, \tag{1}$$

which is proportional to the antenna gain [5], [9]–[11]. Critical sampling of the transmit and receive apertures allows the system to be modeled in the aperture domain as

$$\mathbf{r} = \mathbf{H}\mathbf{x} + \mathbf{w} \tag{2}$$

where $\mathbf{x} = [x(1), \ldots, x(n_T)]^T$ is the transmitted aperture domain signal vector, $\mathbf{r} = [r(1), \ldots, r(n_R)]^T$ is the received aperture domain signal vector, $\mathbf{H}$ is the $n_R \times n_T$ aperture domain channel matrix representing the *propagation channel* coupling the transmitter and receiver antennas, and $\mathbf{w}$ is a $n_R \times 1$ vector representing noise and interference. The model (2) serves as a *direct representation* for conventional MIMO systems with critically spaced discrete antenna arrays, and as a *virtual model* for continuous aperture systems, such as CAP-MIMO, with no loss of information [5], [12].

A. Optimal Beamspace Communication

Modulation of data onto orthogonal basis waveforms is a fundamental concept in communication theory, and *orthogonal spatial beams* form an optimal basis for the *spatial* dimension [5], [9], [10]. In particular, the spatial signal space of an antenna of dimension n can be associated with n orthogonal beams. The aperture domain system model (2) can be equivalently represented in beamspace as

$$\mathbf{r}_b = \mathbf{H}_b\mathbf{x}_b + \mathbf{w}_b \ , \ \mathbf{H}_b = \mathbf{U}_{b,R}^T\mathbf{H}\mathbf{U}_{b,T} \tag{3}$$

where $\mathbf{x}_b = [x_b(1), \ldots, x_b(n_T)]^T$ is the transmitted beamspace signal vector, $\mathbf{r}_b = [r_b(1), \ldots, r_b(n_R)]^T$ is the received beamspace signal vector, $\mathbf{H}_b$ is the $n_R \times n_T$ *beamspace channel matrix* that represents the coupling between the spatial beams at the transmitter and receiver, $\mathbf{U}_{b,T}$ is the $n_T \times n_T$ *transmit beamforming matrix*, $\mathbf{U}_{b,R}$ is $n_R \times n_R$ the *receive beamforming matrix*, and $\mathbf{w}_b = \mathbf{U}_{b,R}^T\mathbf{w}$ is the $n_R \times 1$ beamspace noise vector.

The transmitted (aperture) signal vector is related to the beamspace signal vector as $\mathbf{x} = \mathbf{U}_b\mathbf{x}_b = \sum_{i=1}^n \mathbf{u}(\theta_i)x_b(i)$. Each of the n beamspace signals, $x_b(i)$, is mapped onto a corresponding orthogonal beam represented by a column $\mathbf{u}(\theta_i)$ of $\mathbf{U}_b$. These n beams cover the entire (one-sided) spatial horizon, $-\pi/2 \le \phi \le \pi/2$, where ϕ is the spatial angle relative to broadside. Each $\mathbf{u}(\theta)$ is an array steering/response vector, or array factor, that represents an (all-phase) complex spatial sinusoid whose frequency, $-1/2 \le \theta \le 1/2$, is related to the physical angle ϕ via

$$\theta = \frac{d}{\lambda}\sin(\phi) = \frac{1}{2}\sin(\phi) \tag{4}$$

where $d = \lambda/2$ denotes the aperture domain sample spacing. The n elements of $\mathbf{u}(\theta)$ are given by

$$u_i(\theta) = e^{-j2\pi\theta i}, \ i \in \mathcal{I}(n) = \{i-(n-1)/2 : i = 0, \cdots, n-1\} \tag{5}$$

where $\mathcal{I}(n)$ is a set of n indices symmetrically arranged around the origin. For critical sampling, $d = \lambda/2$, there is a one-to-one mapping between $\theta \in [-1/2, 1/2]$ and $\phi \in [-\pi/2, \pi/2]$. If the spatial frequencies/directions for the n beams, θ_i, are uniformly spaced with spacing

$$\Delta\theta_o = \frac{1}{n} = \frac{\lambda}{2L} \Longleftrightarrow \Delta\phi_o \approx \frac{\lambda}{L} \tag{6}$$

then the resulting $\mathbf{u}(\theta_i)$ are orthogonal to each other. We note that $\Delta\theta_o \leftrightarrow \Delta\phi_o$ is a measure of the spatial resolution or beamwidth of an critically spaced n-element array of length L [9], [13]. $\mathbf{U}_b$ is explicitly constructed with orthogonal $\mathbf{u}(\theta_i)$ column vectors as

$$\mathbf{U}_b = \mathbf{U}_{dft} = \frac{1}{\sqrt{n}}[\mathbf{u}(\theta_i)]_{i\in\mathcal{I}(n)} \ , \ \theta_i = i\Delta\theta_o = \frac{i}{n} \tag{7}$$

which is the $n \times n$ unitary discrete Fourier transform (DFT) matrix, $\mathbf{U}_{dft}^H\mathbf{U}_{dft} = \mathbf{U}_{dft}\mathbf{U}_{dft}^H = \mathbf{I}$, and the physical angles ϕ_i corresponding to the θ_i are the orthogonal spatial angles that cover the entire spatial horizon $\phi \in [-\pi/2, \pi/2]$ [9], [10].

B. Beamspace Channel Modeling

The array steering vector defined in (5) can also be used to define the channel and gain insight into the nature of the low-dimensional communications subspace. For a P2P LoS link, the received aperture domain signal can be related to the signal at i^{th} transmitter sample point by the $n_R \times 1$ steering vector $\mathbf{u}_R(\theta_{ch,i})$, where $\theta_{ch,i}$ is the spatial frequency corresponding to the angle subtended by the i^{th} transmit sample point. The channel is constructed with the $\mathbf{u}_R(\theta_{ch,i})$ column vectors as [9], [10]

$$\mathbf{H}_{los} = \left[\mathbf{u}_R\left(\theta_{ch,i}\right)\right]_{i\in\mathcal{I}(n_T)} \ , \ \theta_{ch,i} = i\frac{\lambda}{4R}. \tag{8}$$

The spacing between the channel frequencies, $\frac{\lambda}{4R}$, is much smaller than the orthogonal spacing, $\Delta\theta_o = \frac{1}{n} = \frac{\lambda}{2L}$, so the channel vectors will be correlated and the channel will be low rank. The channel rank can be approximated by the number of beams that couple strongly between the transmitter and receiver. This is calculated by considering the spatial bandwidth of the receive aperture, $2\theta_{max}$, where $\theta_{max} = 0.5\sin\left(\phi_{max}\right) \approx \frac{L_R}{4R}$ [9], [10]. Thus

$$p_{los,1D} = \frac{2\theta_{max}}{\Delta\theta_o} \approx \frac{L_R}{2R\Delta\theta_o} \approx \frac{L_T L_R}{R\lambda} \tag{9}$$

orthogonal beams, with beamwidth $\Delta\theta_o$, will couple strongly from transmit to receive, where p_{los} is a fundamental quantity known as the Fresnel number in optics [14]. In general, $p_{los} \ll n_T, n_R$ due the relatively large link length, $R \gg L_T, L_R$, which limits the angular extent of the receive aperture. We note that $p_{los,1D}$ is a conservative estimate. In general $p \in [p_{los,1D}, p_{los,1D}+1]$ orthogonal beams will couple strongly. This will be revisited in Sec. IV.

For 2-D planar apertures with $A = L_x \times L_y$ the channel matrix is the Kronecker product of 1-D channels consisting of a transmit antenna of length $L_{T,x}$ or $L_{T,y}$, a receive antenna of length $L_{R,x}$ or $L_{R,y}$, and link length R [9]. This results in

$$n_{2D} = \frac{4A}{\lambda^2} = n_x \times n_y \ , \ p_{los,2D} = \frac{A_T A_R}{R^2\lambda^2} = p_{los,x} \times p_{los,y}. \tag{10}$$

In the case of multipath, the channel can be modeled as [5]:

$$\mathbf{H}_{mp} = \sum_{i=1}^{N_p} \beta_i \mathbf{u}_R(\theta_{R,i})\mathbf{u}_T^H(\theta_{T,i}) \tag{11}$$

where N_p is the number of propagation paths, $\theta_{T,i}$ is the angle of departure, $\theta_{R,i}$ is the angle of arrival, and β_i is the complex gain of the i^{th} path. Here the low dimension of the communication subspace is less readily apparent. However, since we expect the propagation paths to be sparse at mm-wave [2], [15], due to the highly directional nature of propagation and clustered scattering, the propagation paths will only lie within $p_{mp} \ll n_T, n_R$ orthogonal beams (see the concept of virtual path partitioning in [5]).

In general, $\mathbf{H}$ will be a combination of LoS and multipath components with $p = p_{los} + p_{mp}$. However, since LoS propagation plays an important role in mm-wave propagation, for the remainder of the paper we will focus on LoS links where $\mathbf{H} = \mathbf{H}_{los}$, $p = p_{los}$, and $p_{los} > 1$.

A beamspace channel matrix ($\mathbf{H}_b$) corresponding to a DLA-based LoS link with 1D antennas, with $n_T = n_R = 26$ and $p = p_{los} = 2$, is illustrated in Fig. 1. These link specifications are derived from the prototype discussed in Sec. III-D. There are two key observations. First, only a $p \times p$ sub-matrix $\tilde{\mathbf{H}}_b$ of the 26×26 matrix $\mathbf{H}_b$ is non-zero, reflecting the p dimensional communication subspace. Second, $\tilde{\mathbf{H}}_b$ is nearly diagonal indicating that the orthogonal Fourier spatial basis vectors used for beamforming in $\mathbf{U}_b$ (and approximated by the DLA) serve as approximate eigenfunctions of the LoS channel. We will return to these observations in Sec. IV.

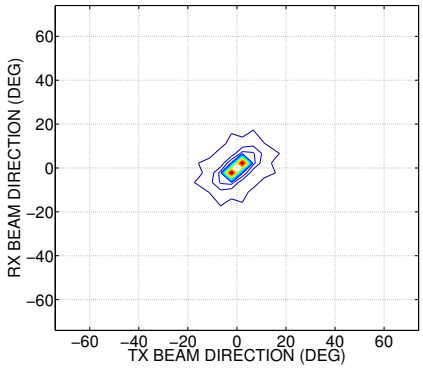

Fig. 1: Normalized Contour plot (30 levels) of $|\mathbf{H}_b|^2$ for a 1D DLA-based link with $n_T = n_R = 26$ and $p = 2$

C. Performance Gains

The advantages of CAP-MIMO lie in its ability to optimally exploit the spatial dimension at mm-wave, through high antenna gain proportional to n and spatial multiplexing of data streams over the p dimensional communication subspace. Basic CAP-MIMO theory developed in [9], [10] provides accurate and insightful closed-form capacity approximations to compare CAP-MIMO with the current state-of-the-art in LoS mm-wave communication. Consider a P2P LoS link with identical transmit and receive antennas of dimension n that can support $p \ll n$ communication modes. For a given operating transmit SNR (ratio of the total transmit signal power to the received noise variance), denoted by ρ, the capacity of CAP-MIMO can be approximated as

$$C_{CAP-MIMO} \approx p\log_2(1+\rho_{rx}) \text{ bits/s/Hz} \tag{12}$$

where the leading p term reflects the spatial multiplexing gain, and $\rho_{rx} = \rho\frac{n^2}{p^2}$ reflects the receive SNR gain, $G = \frac{n^2}{p^2}$ over the receive SNR of an isotropic antenna, ρ. An intuitive interpretation of the receive SNR gain is $G = \frac{1}{p} \times n \times \frac{n}{p}$ reflecting the equal division of transmit SNR among the p beams, the transmit array gain n, and the receive array gain $\frac{n}{p}$ (approximately p orthogonal beams are packed into the receive aperture).

The capacity of the current state-of-the-art mm-wave systems, with the same antenna size and frequency, can be considered as a special case of (12). Continuous aperture "Dish" systems possess high antenna gain, but no spatial multiplexing

gain, so the leading p term is dropped and $\rho\frac{n^2}{p} \leq \rho_{rx} \leq \rho n^2$. The lower bound corresponds to $p_{los} > 1$ and the upper bound to $p_{los} \leq 1$. Conventional widely spaced MIMO uses p discrete antennas, each with gain G_{MIMO} [6]–[9]. This results in full spatial multiplexing gain but reduced SNR gain $\rho_{rx} = \rho G_{MIMO}^2$, $1 \leq G_{MIMO} < \frac{n}{p}$. The upper bound on G_{MIMO} reflects the fact that the discrete antennas must be smaller than $1/p^{th}$ of the aperture.

Fig. 2 compares the capacity of the three systems ($G_{MIMO} = 25$dB) for a LoS link consisting of planar antennas with $40\text{cm} \times 40\text{cm}$ apertures, operating at $f_c = 80$GHz, separated by a link length $R = 42.67$m (e.g., a mm-wave backhaul link), resulting in $p = (p_{los,1D} + 1)^2 = 4$ and $n = 45369$. As evident, CAP-MIMO can deliver significant capacity/SNR gains relative to the state-of-the-art. In particular, CAP-MIMO can achieve a capacity of 10-20 bits/s/Hz with a power advantage of 17-31dB. This corresponds to a data rate of 10-200 Gbps with 1-10GHz system bandwidth. Additionally the capacity of a Dish system using the same aperture size and link length operating at 3GHz ($n = 64$ $p = 1$) is included for reference. While the capacity of the 3GHz link is exceeded at 80GHz by both Dish (through higher antenna gain) and conventional widely spaced MIMO (through spatial multiplexing but with reduced antenna gain), CAP-MIMO is able to leverage both spatial multiplexing and the full antenna gain to obtain the most improvement.

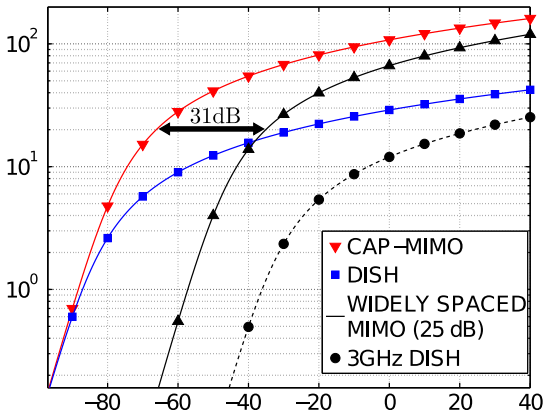

Fig. 2: Approximate capacity plots for CAP-MIMO, Dish, and widely spaced conventional MIMO

D. Transceiver Complexity: Analog vs Digital Beamforming

Fig. 3 shows a conventional MIMO transceiver with a critically spaced discrete antenna array and *digital beamforming* via $\mathbf{U}_{dft}$ where each orthogonal beam is associated with a distinct input to $\mathbf{U}_{dft}$. Alternatively, Fig. 4 shows a CAP-MIMO transceiver using a continuous DLA antenna for *analog beamforming* where each orthogonal beam is associated with a distinct feed antenna on the DLA focal surface. Both systems have the same signal space dimension n and consist of four main functional blocks: i) **DSP** (digital signal processor), ii) **beam selector**, iii) **transceiver hardware** consisting of analog-to-digital/digital-to-analog (A-D/D-A) converters and transceiver (T/R) modules, and iv) **beamformer** (represented by the matrix $\mathbf{U}_{dft}$ in conventional MIMO and $\mathbf{U}_{dla} \approx \mathbf{U}_{dft}$ in CAP-MIMO). We note that in conventional MIMO, blocks ii) and iv) are part of the overall DSP and in CAP-MIMO they represent mm-wave analog devices. For a link with a p dimensional communication subspace, both transceivers map p digital data streams $x_d(1) \ldots x_d(p)$ onto the p orthogonal beams that span the communication subspace.

A key observation is that conventional MIMO has an individual T/R chain associated with each of its n discrete antenna elements regardless of p. On the other hand, CAP-MIMO has a T/R chain associated with each of the p DLA feed antennas corresponding to the p orthogonal beams that span the low dimensional communication subspace. This critical, yet subtle difference leads to a dramatic decrease in the system complexity from the order of n $(10^3 - 10^5)$ in conventional MIMO to the order of p $(2 - 100)$ in CAP-MIMO.

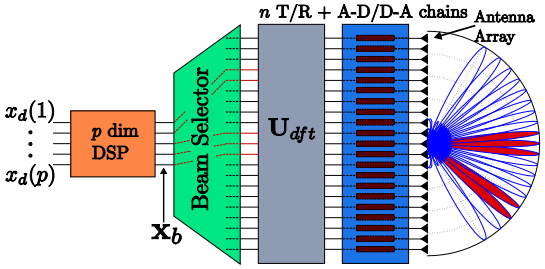

Fig. 3: Digital beamforming in a conventional MIMO transceiver

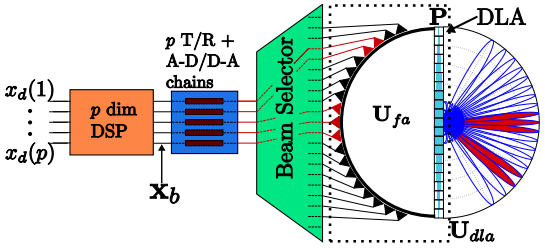

Fig. 4: DLA-based analog beamforming in a CAP-MIMO transceiver

Fig. 4 also illustrates the key elements of the DLA. The DLA is modeled as $\mathbf{U}_{dla} = \mathbf{P}\mathbf{U}_{fa}$, where $\mathbf{P}$ represents the aperture phase profile, and $\mathbf{U}_{fa}$ represents the propagation from the focal antennas to the (critically-sampled) DLA aperture elements. The DLA acts like a convex lens and maps the signals in different directions to different locations on the focal surface. Conventional DLA designs use arrays of receiving and transmitting antennas connected with variable-length transmission line, e.g [16]–[18] or extensions of this concept [19]–[22], to create the aperture phase profile. The high-resolution, low-loss DLA used in CAP-MIMO is composed of sub-wavelength, non-resonant phase shifting elements, or pixels, that can be distributed on a planar surface, and act as bandpass filters [23]. The response of each pixel is tuned to achieve a desired aperture phase profile. The DLA was chosen over alternative analog beamformers, e.g. Butler matrices [24]–[26], because of its low loss and relative ease of construction for antennas with a high dimensional spatial signal space.

In the following sections, we discuss the computational modeling of the DLA-based CAP-MIMO architecture, performance analysis, and measurements performed on a prototype system to validate and refine the promising results given by the basic CAP-MIMO theory.

III. Computational Modeling

In this section, we build on the idea of critical sampling to outline a computational modeling framework for a LoS CAP-MIMO system. Sec. III-A develops a model for the aperture domain channel based on the physical parameters of the link. In Sec. III-B, we develop a critically sampled model for the DLA. In Sec. III-C we combine the channel and DLA models to develop a beamspace model for the DLA-based CAP-MIMO system. Finally, in Sec. III-D we present some illustrative applications of the computational modeling framework to the prototype system.

A. Aperture Domain Channel Modeling

Consider a LoS link consisting of a rectangular transmitter antenna with area $A_T = L_{T,x} \times L_{T,y}$ and dimension $n_T = n_{T,x} \times n_{T,y}$, and a rectangular receiver antenna with area $A_R = L_{R,x} \times L_{R,y}$ and dimension $n_R = n_{R,x} \times n_{R,y}$, separated by a link length of R. The transmit antenna is oriented in the x-y plane with its center at the origin, and the receive antenna is parallel to the transmitter with its center located at a distance R, as shown in Fig. 5. Let $\gamma_T = (x_T, y_T, z_T = 0)$ and $\gamma_R = (x_R, y_R, z_R = R)$ denote the coordinates of points on the transmitter and receiver apertures, respectively. Modeling

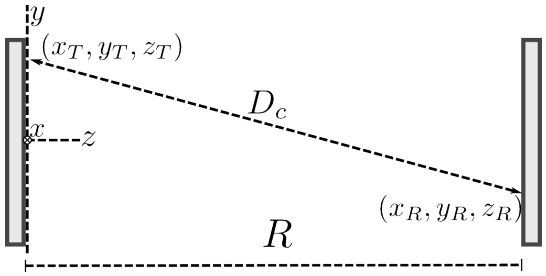

Fig. 5: The LoS link geometry

the aperture points as idealized isotropic antennas and ignoring path loss, the signal at the receiver aperture location, γ_R, is related to the signal at the transmitter aperture location, γ_T, via a pure phase shift, $e^{-j\frac{2\pi}{\lambda}D_c(\gamma_R,\gamma_T)}$, where $D_c(\gamma_R,\gamma_T) = \sqrt{(x_T - x_R)^2 + (y_T - y_R)^2 + R^2}$ is the distance between the two points. The elements of the $n_R \times n_T$ aperture domain channel matrix $\mathbf{H}$ consist of all such pairwise channel phase shifts corresponding to the $\lambda/2$-spaced x-y sample points:

$$H(\ell, m) = e^{-j\frac{2\pi}{\lambda}D_c(\gamma_R(\ell),\gamma_T(m))} \ . \tag{13}$$

The n_T and n_R critically sampled transmitter and receiver coordinates are given by

$$\gamma_T(m) = \gamma_T(m_x, m_y) = \left(\frac{m_x\lambda}{2}, \frac{m_y\lambda}{2}, 0\right), \tag{14}$$

$$\gamma_R(\ell) = \gamma_R(\ell_x, \ell_y) = \left(\frac{\ell_x\lambda}{2}, \frac{\ell_y\lambda}{2}, R\right), \tag{15}$$

where $m = (m_x, m_y) \in \mathcal{I}(n_{T,x}) \times \mathcal{I}(n_{T,y})$, $\ell = (\ell_x, \ell_y) \in \mathcal{I}(n_{R,x}) \times \mathcal{I}(n_{R,y})$, and the index set $\mathcal{I}(n)$ is defined in (5). Using the above transmit and receive aperture sample points in (13) constructs the aperture domain all-phase channel matrix $\mathbf{H}$ that completely characterizes the LoS link. As in (8), each column of $\mathbf{H}$ represents the phase relationship between the signal at a transmit sample point to all the receive sample points. However, (13) accounts for the curvature of the phase front at the receiver unlike the plane wave approximation in (8). Strictly speaking, (13) does not correspond to the Kronecker product of two 1D channels. However, as we will discuss in Sec. IV, it does exhibit a nearly Kronecker structure.

B. DLA Modeling

We now construct a physically accurate model for the DLA matrix, $\mathbf{U}_{dla}$. We consider a DLA in the transmit mode: $\mathbf{U}_{dla}$ represents the mapping from the focal surface antennas to the critically sampled points on its aperture. In the receive mode, the mapping from the aperture to the focal antennas is given by $\mathbf{U}_{dla}^T$. As in Sec. II, the DLA is modeled as $\mathbf{U}_{dla} = \mathbf{P}\mathbf{U}_{fa}$, where $\mathbf{P}$ models the aperture phase profile, and $\mathbf{U}_{fa}$ models the propagation from the focal surface antennas to the aperture. Based on the CAP-MIMO theory, an ideal DLA affects a spatial Fourier transform: $\mathbf{U}_{dla} = \mathbf{U}_{dft}$. In reality, this relationship is approximate. Both $\mathbf{U}_{fa}$ and $\mathbf{P}$ provide design degrees of freedom for improving this approximation.

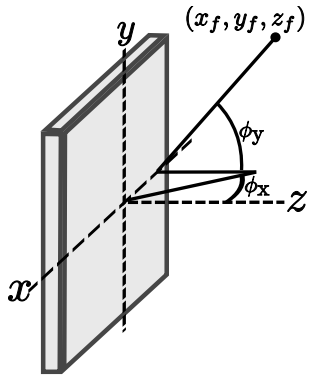

Fig. 6: DLA geometry with feed angles ϕ_x and ϕ_y

Starting with $\mathbf{U}_{fa}$, consider a rectangular DLA with aperture size $A = L_x \times L_y$, dimension $n = n_x \times n_y$, and focal length F, as shown in Fig. 6. The DLA aperture is oriented in the x-y plane with its center at the origin and with the feed antennas located on a focal surface at a radial distance F from the origin. Let $\gamma_a = (x_a, y_a, z_a = 0)$ and $\gamma_f = (x_f, y_f, z_f)$ denote the coordinates of arbitrary points on the aperture and the focal surface. Using Fig. 6, for a given F, we parameterize the focal surface coordinates in terms of the angles ϕ_x and ϕ_y:

$$z_f = \frac{F}{\sqrt{\tan(\phi_x)^2 + \tan(\phi_y)^2 + 1}}$$
$$x_f = z_f \tan(\phi_x) \ , \ y_f = z_f \tan(\phi_y) \ . \tag{16}$$

Modeling the aperture and focal surface points as idealized isotropic antennas, and ignoring path loss, the signal at the aperture location, γ_a, is related to the signal at the focal surface location, γ_f, via a pure phase shift: $e^{-j\frac{2\pi}{\lambda}D_{fa}(\gamma_a,\gamma_f)}$

where $D_{fa}(\gamma_a,\gamma_f)=\sqrt{(x_f-x_a)^2+(y_f-y_a)^2+z_f^2}$ is the distance between the aperture and focal surface points. The elements of the $n\times n$ matrix $\mathbf{U}_{fa}$ consist of all such pairwise phase shifts corresponding to the critically spaced aperture and focal surface points:

$$U_{fa}(\ell,m)=\frac{1}{\sqrt{n}}e^{-j\frac{2\pi}{\lambda}D_{fa}(\gamma_a(\ell),\gamma_f(m))} \tag{17}$$

where the $1/\sqrt{n}$ term is used for power normalization. The n critically sampled aperture coordinates are given by

$$\gamma_a(\ell)=\gamma_a(\ell_x,\ell_y)=\left(\frac{\ell_x\lambda}{2},\frac{\ell_y\lambda}{2},0\right)\ , \tag{18}$$

where $\ell=(\ell_x,\ell_y)\in\mathcal{I}(n_x)\times\mathcal{I}(n_y)$. The critically sampled focal surface coordinates, $\gamma_f(m)=\gamma_f(m_x,m_y)$, are determined by choosing the angles $\phi_x(m_x)$ and $\phi_y(m_y)$ to be the 1D orthogonal spatial angles defined in (6) and (4):

$$\begin{aligned}\phi_x(m_x)&=\sin^{-1}(2\theta_x(m_x))\ ,\theta_x(m_x)=\frac{m_x}{n_x}\\ \phi_y(m_y)&=\sin^{-1}(2\theta_y(m_y))\ ,\theta_y(m_y)=\frac{m_y}{n_y}\ ,\end{aligned} \tag{19}$$

where $m_x\in\mathcal{I}(n_x)$ and $m_y\in\mathcal{I}(n_y)$. We note that the focal surface coordinates in (16), parameterized by the angles in (19), determine the location of the DLA feed antennas. Combining these coordinates with the aperture coordinates given by (18) in (17) yields the matrix $\mathbf{U}_{fa}$. Each column of $\mathbf{U}_{fa}$ represents the phase relation between a particular feed signal and all the aperture sample points, and the power normalization ensures power conservation between the feed antenna and the DLA aperture.

For a given $\mathbf{U}_{fa}$, the aperture phase profile matrix $\mathbf{P}$ is designed so that $\mathbf{U}_{dla}$ best approximates $\mathbf{U}_{dft}$. This is, in general, a complex problem and relates to the significant work on microwave lenses over several decades [16]–[22]. For our initial prototype, we work with the simplest *broadside* DLA design in which a plane wave coming from the broadside direction is perfectly focused on the broadside feed location or vice versa. This requires that the phase shift from the broadside feed location to any point on the DLA aperture is constant. At an arbitrary aperture location, $\gamma_a=(x_a,y_a,z_a=0)$, this phase shift, $\psi(\gamma_a)$, is given by

$$\begin{aligned}\psi(\gamma_a)&=\delta_{max}-\delta(\gamma_a)\ ,\ \delta(\gamma_a)=\frac{2\pi}{\lambda}\sqrt{x_a^2+y_a^2+F^2}\\ \delta_{max}&=\frac{2\pi}{\lambda}\sqrt{\frac{L_x^2}{4}+\frac{L_y^2}{4}+F^2}.\end{aligned} \tag{20}$$

Assuming that the different sample points or DLA pixels do not interact, which is the assumption in our DLA design [23], $\mathbf{P}$ is a diagonal matrix. Assuming that the DLA aperture is lossless, the diagonal elements of $\mathbf{P}$ are given by the phase shift ψ at the critically spaced aperture sample points:

$$P(\ell,\ell)=e^{-j\psi(\gamma_a(\ell))}\ ,\ \ell=(\ell_x,\ell_y)\in\mathcal{I}(n_x)\times\mathcal{I}(n_y)\ , \tag{21}$$

where $\gamma_a(\ell)$ is defined in (18).

We have outlined the constructions for $\mathbf{U}_{fa}$ and $\mathbf{P}$ in terms of *critically spaced* aperture and focal surface samples, which is the minimum sampling resolution required for accurate system modeling, consistent with the dimension of the spatial signal space. While finer (higher resolution) sampling may be employed for visualization purposes, critically sampling is sufficient for the system analysis in Sec. IV.

C. Beamspace System Modeling

We are now in a position to model the complete DLA-based CAP-MIMO system in beamspace. Consider a LoS link of length R connected by planar antennas of dimensions n_T and n_R. Using the aperture domain channel matrix $\mathbf{H}$ in (13) the aperture domain system is described by (2). The beamspace channel model is given by (3), characterized by the $n_R\times n_T$ beamspace channel matrix $\mathbf{H}_b$, where $\mathbf{U}_{b,T}$ and $\mathbf{U}_{b,R}$ denote the transmit and receive beamforming matrices. For an ideal CAP-MIMO system, the beamforming matrices are given by the DFT matrices, defined in (7). For an actual DLA-based CAP-MIMO system, the beamforming matrices are given by $\mathbf{U}_{dla}=\mathbf{P}\mathbf{U}_{fa}$ using the constructions in (17) and (21).

As discussed in Sec. II, for a LoS link $p=p_{los}\ll n_T,n_R$ beams, defined in (10), strongly couple from the transmitter to the receiver and represent the communication modes of the link. In a CAP-MIMO system, these modes are accessed via beams that are in turn accessed via a subset of the focal surface feed antennas in a DLA-based system. Thus, in subsequent sections, we explicitly consider such lower dimensional system representations corresponding to a subset of n_b DLA feed antennas or beams. Let $\tilde{\mathbf{U}}_{b,T}$ and $\tilde{\mathbf{U}}_{b,R}$ represent the corresponding $n_T\times n_b$ and $n_R\times n_b$ beamforming sub-matrices obtained by retaining the columns corresponding to the selected beams. The corresponding $n_b\times n_b$ beamspace channel matrix is given by $\tilde{\mathbf{H}}_b=\tilde{\mathbf{U}}_{b,R}^T\mathbf{H}\tilde{\mathbf{U}}_{b,T}$. In particular, for the DLA-based system

$$\tilde{\mathbf{H}}_b=\tilde{\mathbf{U}}_{dla,R}^T\mathbf{H}\tilde{\mathbf{U}}_{dla,T}=\tilde{\mathbf{U}}_{fa,R}^T\mathbf{P}^T\mathbf{H}\mathbf{P}\tilde{\mathbf{U}}_{fa,T} \tag{22}$$

where $\tilde{\mathbf{U}}_{fa,T}$ ($n_T\times n_b$) and $\tilde{\mathbf{U}}_{fa,R}$ ($n_R\times n_b$) denote the transmit and receive DLA propagation sub-matrices corresponding to the selected n_b feed antennas.

D. The Prototype System

In this section, we apply the basic CAP-MIMO theory and the modeling framework to an actual prototype system that we have built as an initial test platform. The prototype consists of two 40cm $\times$ 40cm square DLAs, designed for broadside focusing with a focal length of $F=40$cm using the procedure in [23], separated by a link length of $R=2.67$m (8.75 ft), and operating at $f_c=10$GHz. While this falls outside of the mm-wave regime $fc\in[30,300]$GHz, the prototype is intended to show spatial multiplexing in a LoS link, as predicted by the CAP-MIMO theory. The results scale to mm-wave where the smaller wavelengths will result in larger link lengths for a given A and p (see Sec. II-C). These specifications were chosen based on the available measurement equipment, and result in system parameters of $n=676$ and $p_{los}=4$ (or 1D parameters of $n_x=n_y=26$ and $p_{los,1D}=2$).

To assess how well the broadside DLA design approximates the ideal DFT operation, we analyze the matrix $\mathbf{U}_{dft}^H\mathbf{U}_{dla}=\mathbf{U}_{dft}^H\mathbf{P}\mathbf{U}_{fa}$. The $(\ell,m)^{th}$ entry of $\mathbf{U}_{dft}^H\mathbf{U}_{dla}$ contains the inner product between the ℓ^{th} and m^{th} columns of $\mathbf{U}_{dft}$ and $\mathbf{U}_{dla}$, representing the corresponding beams. Physically, the

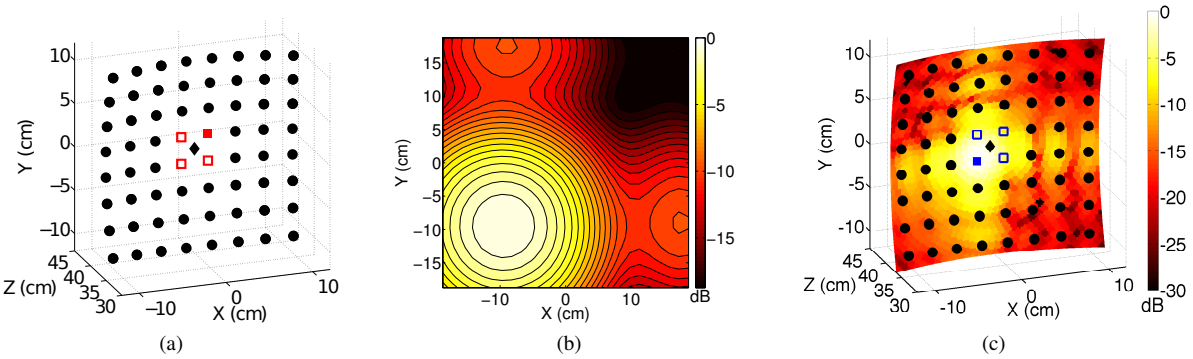

Fig. 8: Tracking beam propagation through the system: (a) shows a subsection of the TX focal surface with the activated feed indicated by the filled red square, (b) shows the resulting aperture domain receive signal radiation intensity pattern, and (c) shows the RX focal surface radiation intensity pattern with the active feed shown as a filled blue square. In (a) and (c) broadside is indicated by a black diamond.

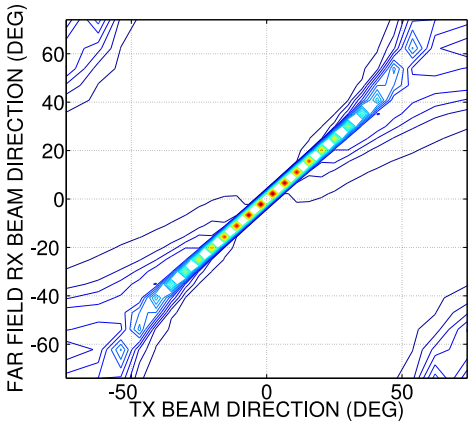

Fig. 7: Contour plot of $|\mathbf{U}_{dft}^H \mathbf{U}_{dla}|^2$ for assessing how well $\mathbf{U}_{dla}$ approximates the ideal $\mathbf{U}_{dft}$

$(\ell, m)^{th}$ entry represents the coupling from the (isotropic) m^{th} DLA feed antenna to an isotropic sensor placed at the ℓ^{th} orthogonal beam direction in the far-field. For a perfectly designed DLA, we expect the matrix to be diagonal - the identity matrix; that is, ideally, the m^{th} feed antenna should only couple with the corresponding m^{th} orthogonal beam. Fig. 7 shows a contour plot of $|\mathbf{U}_{dft}^H \mathbf{U}_{dla}|^2$ for the 1D case ($n_{1D} = 26$) consisting of linear antennas. As evident, the broadside DLA closely approximates the DFT for physical angles between ± 30 degrees (which contains 14 orthogonal beams) and exhibits some off-diagonal entries beyond that range. Thus, the broadside DLA design seems quite adequate for broadside links with p_{los} up to 10. We will revisit this observation in Sec. V.

Next we use the modeling framework to track the propagation of one of the p_{los} beams that span the communication subspace through the system to gain a qualitative understanding of CAP-MIMO's operation. As shown in Fig. 8, the propagation proceeds as follows: i) Fig. 8a shows a sub-section of the transmit DLA focal surface with the p_{los}=4 selected feed locations (corresponding to the orthogonal beams that span the communication subspace) shown as red squares with the activated feed filled in, ii) Fig. 8b shows the receive aperture radiation intensity, given by $|\mathbf{H}\mathbf{u}_{dla}|$ where $\mathbf{u}_{dla}$ is the column of $\mathbf{U}_{dla}$ corresponding to the activated feed, iii) Fig. 8c shows the receive focal surface radiation intensity with the selected feeds shown as blue squares and the active feed filled in. As evident the received aperture signal is concentrated in one quadrant of the aperture and the received beamspace signal is concentrated on the intended feed with most of its power concentrated on the selected p_{los} feeds. The signals excited by the other selected feeds will be rotations of this signal, demonstrating how CAP-MIMO packs $p_{los} = 4$ independent beams into the receiver aperture (see also Fig. 1).

While the above discussion applies to idealized isotropic antennas, the modeling framework can be extended to account for the actual feeds used for measurements. Essentially, we need to modify the columns of $\mathbf{U}_{fa}$ which represent the relationship between the signal at a particular feed antenna and the electric field at the critical aperture sample points. Since the focal length F is sufficiently large compared to the size of the feed antennas, whose dimensions are on the order of λ, we can use well-known approximations for the far-field patterns of the chosen feed antennas [13]. The columns of $\mathbf{U}_{fa}$ can be modified by projecting the electric field of the actual feed antennas onto the DLA aperture coordinates, accounting for different feed locations relative to the DLA aperture. The modified columns of $\mathbf{U}_{fa}$ should be normalized to unit energy. This will be further discussed in the Appendix.

IV. Analytical Results

In this section, we use the computational modeling framework to the analyze the performance of CAP-MIMO in a P2P LoS link. In Sec. IV-A, we discuss the LoS link capacity and how it is achieved by CAP-MIMO via beamspace communication. Then in Sec. IV-B, we analyze the capacity of the prototype DLA-based CAP-MIMO system.

A. Link Capacity and Optimal Beamspace Signaling

The LoS link capacity is governed by the eigenvectors and eigenvalues of the $n_R \times n_T$ sampled aperture channel matrix $\mathbf{H}$. Let $n_o = \min(n_R, n_T)$ and $\sigma_c^2 = \mathrm{tr}(\mathbf{H}^H\mathbf{H}) = n_T n_R$ denote the channel power. It is well-known [3] that capacity-

achieving signaling is governed by the singular value decomposition (SVD) of $\mathbf{H}$, $\mathbf{H} = \mathbf{U}_c \mathbf{\Lambda}_c^{1/2} \mathbf{V}_c^H$, where $\mathbf{U}_c$ $(n_R \times n_o)$ is the matrix of eigenvectors of the receive covariance matrix $\mathbf{H}\mathbf{H}^H = \mathbf{U}_c \mathbf{\Lambda}_c \mathbf{U}_c^H$, $\mathbf{V}_c$ $(n_T \times n_o)$ is the matrix of eigenvectors of the transmit covariance matrix $\mathbf{H}^H\mathbf{H} = \mathbf{V}_c \mathbf{\Lambda}_c \mathbf{V}_c^H$, and $\mathbf{\Lambda}_c = \mathrm{diag}(\lambda_1, \cdots, \lambda_{n_o})$ is the matrix of non-negative eigenvalues. In the presence of complex additive white Gaussian noise (AWGN), capacity-achieving signaling consists of independent Gaussian signals over the transmit eigenvectors. That is, the optimal n_T dimensional transmit signal vector $\mathbf{x}$ is complex Gaussian, $\mathbf{x} \sim \mathcal{CN}(\mathbf{0}, \mathbf{V}_c \mathbf{\Lambda}_s \mathbf{V}_c^H)$, with $\mathbf{\Lambda}_s = \mathrm{diag}(\rho_1, \cdots, \rho_{n_o})$ denoting the matrix of eigenvalues of the signal covariance matrix, and $\rho = \mathrm{tr}(\mathbf{\Lambda}_s) = \sum_{i=1}^{n_o} \rho_i$ denoting the total transmit SNR (signal to noise ratio), since the noise variance is taken to be unity without loss of generality. The link capacity is given by the well-known waterfilling power-allocation formula [3], [27]

$$C(\rho) = \max_{\rho_i : \sum_{i=1}^{n_o} \rho_i \le \rho} \log_2[\det(\mathbf{I} + \mathbf{\Lambda}_c \mathbf{\Lambda}_s)] \quad \text{bits/s/Hz} \tag{23}$$

$$= \max_{\rho_i : \sum_{i=1}^{n_o} \rho_i \le \rho} \sum_{i=1}^{n_o} \log_2(1 + \lambda_i \rho_i) \tag{24}$$

$$\approx \max_{\rho_i : \sum_{i=1}^{p_{los}} \rho_i \le \rho} \sum_{i=1}^{p_{los}} \log_2(1 + \lambda_i \rho_i) \tag{25}$$

$$\approx p_{los} \log_2 \left(1 + \rho \frac{n_T n_R}{p_{los}^2}\right) \tag{26}$$

where the approximation in (25) is based on the fact that $\mathbf{H}$ has p_{los} dominant non-zero eigenvalues, and the second approximation, used in (26), is based on the assumption that non-zero eigenvalues are equal ($\lambda_i \approx n_T n_R / p_{los}$) with equal power ($\rho_i = \rho / p_{los}$) allocated to them. In general, p_{los} is a conservative approximation of the number of non-zero eigenvalues, and the eigenvalues are not exactly uniform. At low SNRs, all the power is allocated to the dominant mode corresponding to the largest eigenvalue and additional dominant modes are activated as the SNR increases, with equal power allocated to all the dominant non-zero modes at sufficiently high SNR.

The CAP-MIMO transceiver architecture is based on a key observation that the Fourier basis functions serve as approximate channel eigenfunctions [9], [10] which are in turn approximated by the DLA; that is,

$$\mathbf{U}_c \approx \mathbf{U}_{b,R}^* \approx \mathbf{U}_{dla,R}^* \ , \ \mathbf{V}_c \approx \mathbf{U}_{b,T} \approx \mathbf{U}_{dla,T} \tag{27}$$

and the beamspace channel matrix $\mathbf{H}_b$ is an approximation to the diagonal matrix of channel singular values ($\mathbf{\Lambda}_c^{1/2}$), as illustrated in Fig. 1. Thus, beamspace communication, affected through DLA-based analog beamforming in CAP-MIMO, provides near-optimal access to the p_{los}-dimensional communication subspace of the high-dimensional $n_R \times n_T$ channel $\mathbf{H}$. In particular, a $p_{los} \times p_{los}$ sub-matrix of $\mathbf{H}_b$, $\tilde{\mathbf{H}}_b$, characterizes this low-dimensional communication subspace that is accessed with transceiver complexity on the order of p as shown in Fig. 4. This corresponds to the DSP block modulating each of the p data streams onto a singular vector of $\tilde{\mathbf{H}}_b$. In subsequent sections, we will evaluate the capacities of various systems by using the appropriate set of eigenvalues in (24). We note that capacity achieving signaling requires knowledge of the channel at both the transmitter and receiver. Since we expect the deterministic LoS channel to vary slowly, there will be sufficient time to obtain estimates of the channel at both the transmitter and receiver.

B. Prototype Capacity Analysis

In this section, we theoretically assess the eigenvalues and the capacity of the prototype LoS link described in Sec. III-D ($n = 676$ and $p_{los} = 4$), and the ability of CAP-MIMO to approach capacity with the designed DLA. Fig. 9 shows the 10 largest eigenvalues of $\mathbf{H}^H\mathbf{H}$ and $\mathbf{H}_b^H\mathbf{H}_b$, and 4 eigenvalues of $\tilde{\mathbf{H}}_b^H\tilde{\mathbf{H}}_b$, normalized with respect to the maximum eigenvalue of $\mathbf{H}^H\mathbf{H}$, to compare the number of modes supported by the aperture channel, full-dimensional beamspace channel, and the low-dimensional beamspace channel. All channels exhibit $p_{los} \approx 4$ dominant modes as theoretically expected. Furthermore, the distribution of eigenvalues is very similar to what would be expected from a Kronecker matrix. This confirms that while the channel model (13) is not strictly Kronecker, it behaves very similarly to the insightful array steering vector model (8) used in developing the basic CAP-MIMO theory. We note that the eigenvalues of $\mathbf{H}_b$ are a little higher than the eigenvalues of $\mathbf{H}$ as a consequence of the broadside DLA design.[1]

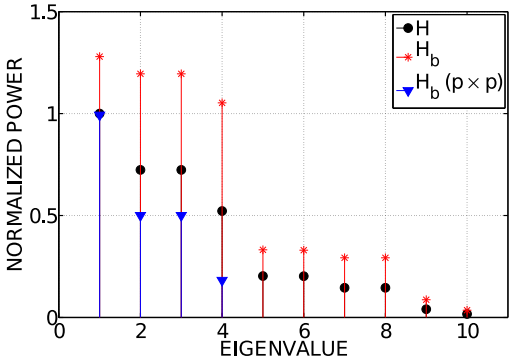

Fig. 9: Theoretical eigenvalues of $\mathbf{H}^H\mathbf{H}$, $\mathbf{H}_b^H\mathbf{H}_b$, and $\tilde{\mathbf{H}}_b^H\tilde{\mathbf{H}}_b$ normalized to the maximum eigenvalue of $\mathbf{H}^H\mathbf{H}$

Using the theoretical eigenvalues, Fig. 10 compares the capacity of the $p_{los} \times p_{los}$ CAP-MIMO system with the two state-of-the-art designs – a single-mode Dish system and the conventional $p_{los} \times p_{los}$ MIMO system with widely spaced antennas – tailored to the prototype specifications. The conventional MIMO antennas have a gain of $G_{MIMO} = 10$dB. The CAP-MIMO gain between broadside feed locations is used as a proxy for the Dish gain. The capacity (bits/s/Hz) is plotted as a function of the transmit SNR - ratio of total transmit power ρ to the unit noise variance at the receiver for all systems. (The absolute SNR values are not critical here - we calibrate them to their physical values in the next section.) In the conventional systems, Dish dominates at low SNRs whereas widely spaced MIMO dominates at high SNRs. CAP-MIMO

[1]This relative increase in beamspace eigenvalues in the broadside LoS link is offset by a reduction in beamspace channel power in off-broadside directions to ensure total power conservation; see Sec. V-B.

outperforms the state-of-the-art over the entire SNR range, reflecting the multiplexing gain over Dish and power gain over conventional MIMO. The results show that at a spectral efficiency of 10 bits/s/Hz, or a data rate of 10 Gbps with 1GHz system bandwidth, CAP-MIMO has a 17dB SNR advantage over the state-of-the-art. Fig. 10 also shows that CAP-MIMO closely approximates the capacity of the 4-beam ideal DFT channel. The capacity of a CAP-MIMO system with $p = 12$ feeds is also shown which more closely approximates the capacity of the full-dimensional (676x676) aperture domain channel $\mathbf{H}$. This underscores two important observations. First, p_{los}, as calculated in (10), is an approximate indicator – larger number of modes can be exploited with higher transceiver complexity. Second, by increasing the number of feeds to 12, CAP-MIMO can approach the full capacity of the LoS link with a dramatically lower complexity (on the order of 12) compared to the order $n = 676$ complexity of a critically-spaced (676x676) conventional MIMO system.

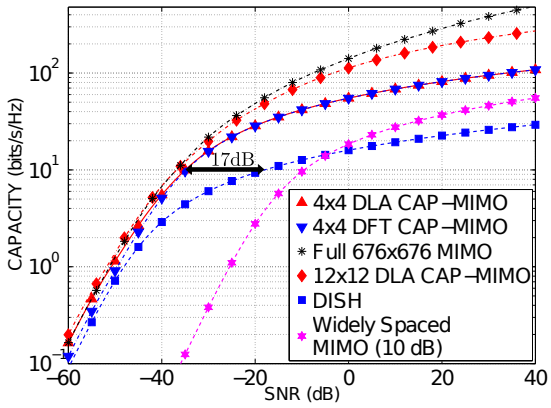

Fig. 10: Capacity comparison between CAP-MIMO and several alternative systems for the prototype LoS link

V. Measurement Results

In this section we discuss the measurement results obtained using the prototype LoS CAP-MIMO system ($n = 676$, $p = p_{los} = 4$) specified in Sec. III-D. The prototype DLAs were constructed using the procedure outlined in [23]. Each DLA consists of 8 dielectric layers and 9 (4 inductive and 5 capacitive) metallic layers with 4489 $\frac{\lambda}{5} \times \frac{\lambda}{5}$ phase shifting pixels. The measurement setup consists of two structures that support the DLAs as shown in Fig. 11. The feed antennas are held by an arm shown in Fig. 12 and moved to the appropriate positions to measure the elements of the $p_{los} \times p_{los}$ beamspace channel submatrix $\tilde{\mathbf{H}}_b$ using a vector network analyzer (VNA). Two types of DLA feed antennas were used for measurements: vertically oriented $\lambda/2$ dipole (DP) antennas, and open-ended WR-90 waveguide (WG) antennas supporting a vertically oriented TE_{10} mode. Sec. V-A discusses the broadside P2P measurements in which the DLAs are facing each other. We compare the measurement results with the theoretical results obtained in Sec. IV to assess the accuracy of the modeling framework. Sec. V-B discusses preliminary measurement results to assess the off-broadside performance of CAP-MIMO relevant to point-to-multipoint (P2MP) links. Finally, Sec. V-C presents system bandwidth measurements.

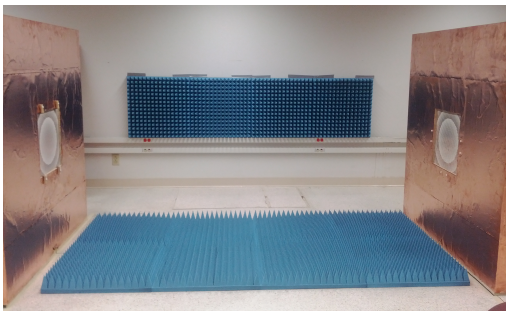

Fig. 11: CAP-MIMO prototype measurement setup

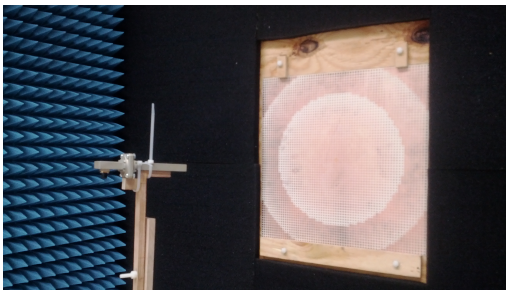

Fig. 12: CAP-MIMO measurement structure showing the feed arm used to perform the measurements.

A. Point-to-Point Measurements

In this section, we discuss P2P measurements taken using both the DP and WG feeds at 10GHz. Let $\hat{\tilde{\mathbf{H}}}_{bm}$ denote the *measured* $p \times p$ beamspace channel submatrix and $\tilde{\mathbf{H}}_{bm}$ denote its theoretical prediction. We want to relate the p eigenvalues of $\tilde{\mathbf{H}}_b$ to the the corresponding eigenvalues of $\tilde{\mathbf{H}}_{bm}$. To address this we consider two key issues: i) calibration of the channel power/eigenvalues of the sampled model in an idealized loss-free system to their actual physical values, and ii) analysis of the dominant sources of power loss in the prototype. Define the following (transmit) covariance matrices with their corresponding eigenvalue decompositions and powers

$$\begin{aligned}
\boldsymbol{\Sigma} &= \mathbf{H}^H\mathbf{H} = \mathbf{U}\boldsymbol{\Lambda}\mathbf{U}^H \ , \ \sigma_c^2 = \mathrm{tr}(\boldsymbol{\Sigma}) \\
\tilde{\boldsymbol{\Sigma}}_b &= \tilde{\mathbf{H}}_b^H\tilde{\mathbf{H}}_b = \tilde{\mathbf{U}}_b\tilde{\boldsymbol{\Lambda}}_b\tilde{\mathbf{U}}_b^H \ , \ \tilde{\sigma}_b^2 = \mathrm{tr}(\tilde{\boldsymbol{\Sigma}}_b) \\
\tilde{\boldsymbol{\Sigma}}_{bm} &= \tilde{\mathbf{H}}_{bm}^H\tilde{\mathbf{H}}_{bm} = \tilde{\mathbf{U}}_{bm}\tilde{\boldsymbol{\Lambda}}_{bm}\tilde{\mathbf{U}}_{bm}^H \ , \ \tilde{\sigma}_{bm}^2 = \mathrm{tr}(\tilde{\boldsymbol{\Sigma}}_{bm}) \ .
\end{aligned}$$

While the losses can vary across modes (orthogonal beams that serve as approximate channel eigenfunctions), we expect the variation to be small for the LoS link. Thus we study the relationship between the *average* channel eigenvalues:

$$\lambda_{ave} = \frac{\sigma_c^2}{p} = \frac{\sum_{i=1}^n \lambda_i}{p} \qquad \tilde{\lambda}_{b,ave} = \frac{\tilde{\sigma}_b^2}{p} = \frac{\sum_{i=1}^p \tilde{\lambda}_{b,i}}{p}$$
$$\tilde{\lambda}_{bm,ave} = \frac{\tilde{\sigma}_{bm}^2}{p} = \frac{\sum_{i=1}^p \tilde{\lambda}_{bm,i}}{p}.$$

To address the first issue, the lossless channel power is calibrated to $\sigma_c^2 = 3.78$ using the analysis in the Appendix. This value reflects the physically meaningful calibration (rather than

n^2 in the system model) that accounts for free-space path loss. To address the second issue, we use the following relationships:

$$\begin{aligned}\tilde{\lambda}_{bm,ave} &= L_T\tilde{\lambda}_{b,ave} = L_P L_{D,T} L_{D,R}\tilde{\lambda}_{b,ave} \\ &= L_P L_{D,T} L_{D,R} L_S \lambda_{ave} \end{aligned} \quad (28)$$

where $L_T = L_P L_{D,T} L_{D,R}$ denotes the total power loss in the system, $\tilde{\lambda}_{b,ave} = L_S\lambda_{ave}$, and the losses have the following interpretation (per mode):

1) L_P represents the fraction of power radiated by the transmitter that couples to the receiver.
2) L_D represents the fraction of power radiated by a DLA feed that couples to the DLA aperture, and vice versa.
3) L_S is the power loss due to limiting our attention to a p-dimensional subspace in beamspace.

Here, $L_{D,T}$ and $L_{D,R}$ refer to the loss at the transmitter and receiver respectively. In broadside P2P links $L_{D,T} = L_{D,R} = L_D$. From the analysis in the Appendix, we get the following values for the different quantities in (28):

$$\lambda_{ave} = 0.94,\ L_S = 0.58,\ L_{P,WG} = 0.61,\ L_{P,DP} = 0.61$$
$$L_{D,WG} = 0.22,\ L_{D,DP} = 0.09$$

where the subscript WG refers to the WR-90 waveguide feed and DP refers to the dipole feed. Using the above values, we obtain the following *theoretical predictions* for average beamspace channel eigenvalues

$$\begin{aligned}\tilde{\lambda}_{b,ave} &= -2.64\text{dB}\ , \\ \tilde{\lambda}_{bm,ave,WG} = -17.72\text{dB}\ &,\ \tilde{\lambda}_{bm,ave,DP} = -26.18\text{dB}\end{aligned} \quad (29)$$

which are used for comparison with the measurement results.

Fig. 13 plots the eigenvalues of the measured and theoretical channels (normalized with respect to each channel's maximum eigenvalue). Both the DP and WG channels exhibit $p = 4$ dominant eigenvalues, as predicted by theory. The un-normalized average eigenvalues for the two channels are

$$\hat{\tilde{\lambda}}_{bm,ave,WG} = -17.67\text{dB}\ ,\ \hat{\tilde{\lambda}}_{bm,ave,DP} = -27.77\text{dB} \quad (30)$$

which are quite close to their theoretically predicted values in (29). We note from Fig. 13 that the DP channel better approximates the theoretical distribution of eigenvalues, likely due to the fact that its radiation pattern better approximates the ideal uniform pattern. On the other hand, from (30) we note that the WG feeds result in significantly better power coupling ($\sim$ 10dB) to the DLA aperture, compared to the DP feeds.

Next we assess the capacity of the measured channels relative to the theoretical predictions. The channel powers for the theoretical channels are normalized to the following values:

1) Lossless: $\tilde{\sigma}_b^2 = L_S\sigma_c^2 = 0.58 \times 3.78 = 2.18$
2) WG: $\tilde{\sigma}_{bm,WG}^2 = L_{D,WG}^2 L_{P,WG}\tilde{\sigma}_b^2 = 0.068$
3) DP: $\tilde{\sigma}_{bm,DP}^2 = L_{D,DP}^2 L_{P,DP}\tilde{\sigma}_b^2 = 0.010$.

Fig. 14 compares the capacity of the measured DP and WG channels relative to the three theoretical channels given above. Thus, the SNR values in Fig. 14 more accurately reflect the operational transmit SNR. The results show an excellent agreement between the theoretical and measurement performance of WG and DP channels. The SNR gap relative to the theoretical lossless performance reflects the power loss incurred by the two kinds of feeds (about 15dB for WG feeds). With WG feeds, the prototype system can deliver a spectral efficiency of 10 bits/s/Hz at an operational SNR $\approx$ 32dB, corresponding to a data rate of 10 Gbps with 1GHz system bandwidth.

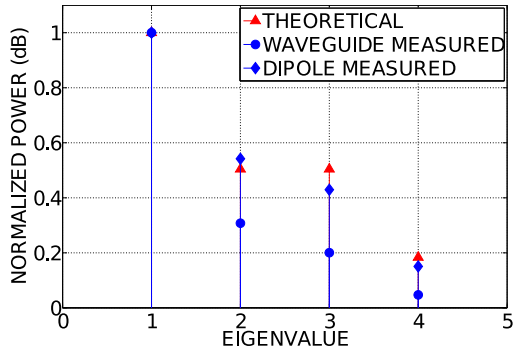

Fig. 13: Normalized eigenvalues of $\tilde{\mathbf{H}}_b$, $\hat{\tilde{\mathbf{H}}}_{bm,WG}$, and $\hat{\tilde{\mathbf{H}}}_{bm,DP}$

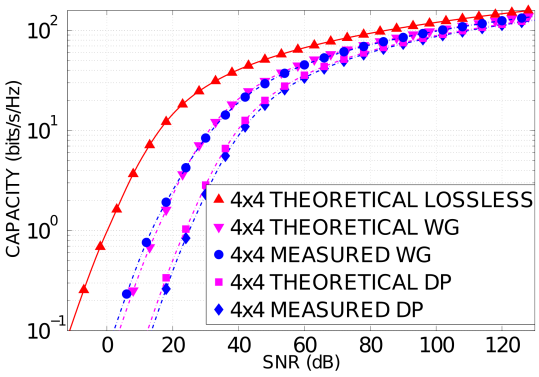

Fig. 14: Capacity versus SNR plots for measured and theoretical values of DP and WG channels. The capacity of the lossless theoretical channel is also included for reference.

B. Point-to-Multi-Point Measurements

A CAP-MIMO transmitter can simultaneously communicate with multiple receivers in a point-to-multipoint (P2MP) network link by appropriately selecting the location and number of feed antennas. Thus, assessment of CAP-MIMO's performance in off-broadside directions is important. Initial off-broadside measurements with WG feeds were made by rotating one of the DLA structures, relative to the broadside direction, as shown in Fig. 15. Channel measurements were made at off-broadside angles up to $\psi = 60$ degrees at 10 GHz to assess P2MP performance over a 120 degree sector. These measurements correspond to a set of P2P links with the transmitter and receiver oriented at different angles.

Fig. 16 plots single-feed off-broadside power measurements and the corresponding theoretical predictions. The measurements were taken by adjusting the feeds so that they were both located along the imaginary line connecting the centers of the DLAs shown in Fig. 15. The results show a fairly good

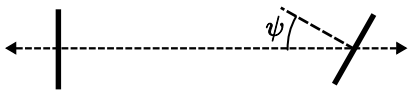

Fig. 15: Top view of the setup used for off-broadside measurements relevant to P2MP operation

agreement between the measured and theoretical values. Both plots are normalized to the value at $\psi = 0$. The theoretical value for each angle is $20\log(|H_b(\psi)|) + 10\log(L_{D,R}(\psi)) + 10\log(L_P(\psi))$ where $H_b(\psi)$ is the scalar beamspace channel between the feeds shown in Fig. 15. $L_P(\psi)$ and $L_{D,R}(\psi)$ are the same as in (28) except that the oblique angle of the receiver is accounted for as discussed in the Appendix. The reflection coefficient was also measured at each angle and varied between approximately -8dB and -10dB. Polarization purity measurements were taken at ψ = 0, 30, 60 degrees by rotating the feed elements so that they would excite/receive horizontally or vertically polarized waves. At each angle the power of the cross-polarized component was at least 19.67dB below the power of the co-polarized component.

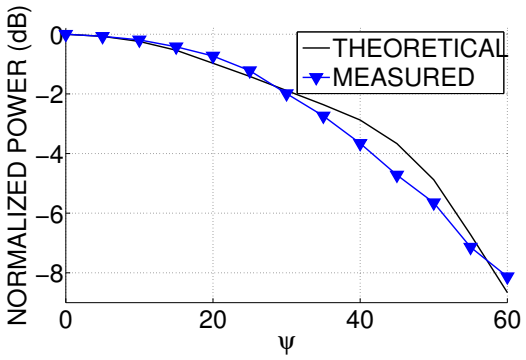

Fig. 16: Single WG feed off-broadside power measurements

Next, 2×2 beamspace channel measurements were performed at ψ =0, 30, 45, 60 degrees, where the two feed locations were in the same horizontal position as in the power measurements but their vertical positions were chosen to correspond to orthogonal beam directions (separated by $\Delta\phi_o$). Table I shows the normalized measured and theoretical eigenvalues of each channel. In addition to showing good agreement, the results show that even at an angle of 60 degrees, the channel possesses 2 dominant eigenvalues. Using the unnormalized eigenvalues, Fig. 17 compares the capacity of the 2×2 channels at different off-broadside angles. While there is some SNR loss in off-broadside directions, a limitation of the current broadside DLA design, the results indicate robust CAP-MIMO P2MP operation over a 120 degree sector.

Eigenvalue	30 degrees	45 degrees	60 degrees
1st Measured/Theoretical	1.00/1.00	1.00/1.00	1.00/1.00
2nd Measured/Theoretical	0.40/0.30	0.28/0.20	0.15/0.11

TABLE I: Normalized measured and theoretical eigenvalues for the 2×2 channel at different off-broadside angles

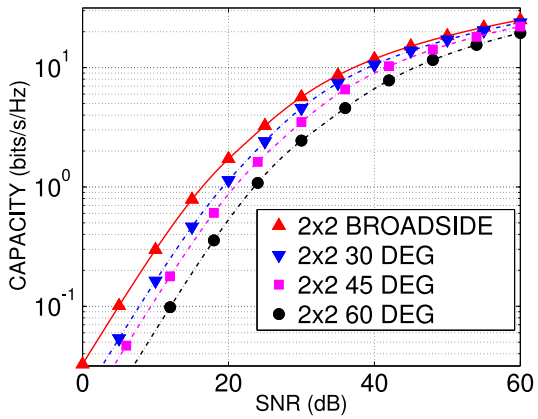

Fig. 17: 2×2 measured channel capacity plots for ψ = 0, 30, 45, 60

C. Bandwidth Assessment

To assess the operational bandwidth of the prototype DLA-based system, bandwidth measurements were made from 8-12GHz using single WG feeds on each end at different angles: $\psi = 0, 30, 45, 60$ degrees. Fig. 18 plots the measurement results with the power normalized to the maximum of the measurements for each angle. Broadside measurements are also shown for DP feeds. The results clearly indicate that the prototype system supports a 3dB bandwidth of at least 1 GHz around $f_c = 10$GHz (10% fractional bandwidth). Since we do not expect the frequency response to change appreciably in the neighborhood of these feed locations, the results are a good indication of the multi-mode system bandwidth for small values of p in both P2P and P2MP operational modes.

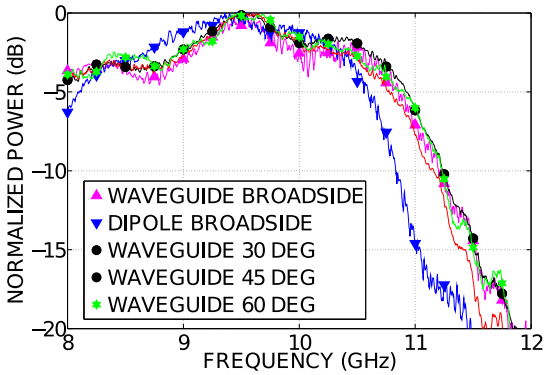

Fig. 18: Prototype frequency response over 8-12GHz for different angles

VI. Conclusions

Mm-wave systems offer a multitude of new opportunities and challenges in the design and analysis of multi-gigabit wireless communication systems. The advantages of relatively small apertures capable of simultaneously supporting high antenna gain and MIMO operation are tempered by the high transceiver complexity associated with optimal exploitation of the spatial dimension in conventional MIMO approaches. In this paper, we have reported promising results on modeling,

analysis, and prototype-based measurements for the recently proposed CAP-MIMO transceiver architecture that exploits the highly directional nature of propagation at mm-wave frequencies through optimal beamspace communication.

A key feature of CAP-MIMO is the analog beamforming spatial front-end that enables near-optimal communication with the lowest transceiver complexity. The computational analysis and prototype-based measurement results reported in this paper reinforce the significant power, capacity and complexity gains of CAP-MIMO over competing state-of-the-art designs predicted by CAP-MIMO theory. The analysis and results also illustrate the utility and accuracy of the underlying computational modeling framework.

The work reported in this paper opens several new avenues for future research on both a system and implementation levels. While the focus of this paper has been on LoS P2P links, the CAP-MIMO architecture is applicable to the whole range of operating conditions: LoS and multipath propagation, P2P and P2MP links, static or mobile links, and wideband operation. While LoS propagation is expected to be the predominant mode of propagation at mm-wave, relatively sparse multipath propagation may be encountered and exploited in indoor [28] and urban [29] environments. The more fruitful exploitation of the spatial dimension in P2MP and multipath channels in general comes at the cost of higher transceiver complexity.

There are several important system implementation-related issues that warrant further investigation. First, DLA designs with more uniform performance across a broader range of angles would be useful for P2MP operation. DLA designs with smaller form factors are also attractive. The large body of work on lens design may be helpful in this regard. Second, the design and analysis of feed antennas is an important issue from the perspective of power efficiency. Third, a related question is the impact of mutual coupling between closely spaced feed antennas, which is not considered in the current computational analysis or measurements. Prior work on the effects of mutual coupling on MIMO performance [30]–[33] could be incorporated into the beamspace modeling framework proposed in this paper. Construction of multi-feed arms will enable the measurement of mutual coupling effects with a multi-port VNA. Investigation of methods for realizing beam selection in an actual transceiver is also an important problem.

APPENDIX

Power Analysis: Reconciling Theory and Measurements

In this appendix, we extend the theoretical results based on the sampled computational model to enable comparison with measurement results. Our focus is on obtaining values for the two power calibration issues given in Sec. V-A.

To calibrate the lossless channel power, σ_c^2, we revisit the Friis transmission formula [34]. Assuming uniform aperture illumination, the gain of a square antenna with area A is given by $G = \frac{4\pi A}{\lambda^2} = \pi n$, which is proportional to the spatial signal space dimension, n. Direct application of the formula to the LoS link results in the following relationship between the transmit power P_T and the received power P_R:

$$\frac{P_R}{P_T} = \frac{G_T}{4\pi R^2} A_R = \frac{G_T G_R \lambda^2}{(4\pi R)^2} = \frac{A_T A_R}{(R\lambda)^2} = p \qquad (31)$$

which is a clearly incorrect since $p = p_{los} > 1$. This seemingly incorrect result is primarily due to the fact that multi-mode communication in LoS propagation requires link lengths that are within the boundary of the conventional far-field definition: $R > \frac{4A}{\lambda}$. Since there are p approximately non-overlapping coupling modes (beams), each mode will only illuminate an area of approximately A_R/p at the receiver (see Fig. 8b). Even within this area, the amplitude of each mode will not be uniform. However, if we take the effective receiver area as A_R/p in (31), we get the more reasonable result that P_R/P_T=1. The above caveats notwithstanding, this interpretation actually yields a meaningful extension of Friis formula to multi-mode transmission. First, it implies that, in an idealized setting, exactly p modes couple the LoS link with no loss of power. Second, it suggests a physically meaningful normalization of the channel power from σ_c^2=$n_T n_R$=n^2 in our theoretical sampled model (which reflects the antenna *gain* relative to isotropic antennas) to $\sigma_c^2 \approx p$ (in the absence of any losses).

To determine the value of λ_{ave} (or equivalently σ_c^2), we use the above discussion to obtain bounds on λ_{ave} and then use the sampled representation to obtain an estimate. For the upper bound, we consider the extreme case in which each of the p modes is uniform over A_R/p portion of the receive aperture and zero everywhere else, with no loss of power. This results in $\tilde{\sigma}_c^2 = p$ and $\lambda_{ave} = 1$. For the lower bound, we assume that the total power is conserved over all modes and each mode suffers a loss of $1/p$: $\sigma_c^2 = 1$ and $\lambda_{ave} = 1/p$. The reality lies somewhere between these two extremes, and we use the sampled channel matrix $\mathbf{H}$ to get a reasonable estimate for λ_{ave}: we keep the p largest eigenvalues of $\mathbf{\Sigma}$ and then normalize them by the largest λ_i. This yields,

$$\lambda_{max} = 1 \ , \ 1 < \sigma_c^2 < p \ , \ 1/p \leq \lambda_{ave} \leq 1. \qquad (32)$$

For our theoretical model for the prototype, we get $\sigma_c^2 = 3.78$ and $\lambda_{ave} = 0.94$.

Now we move to calculating the component losses in (28). The loss L_S is calculated using the theoretical model as

$$L_S = \frac{\tilde{\lambda}_{b,ave}}{\lambda_{ave}} = \frac{\tilde{\sigma}_b^2}{\sigma_c^2} = \frac{\tilde{\sigma}_b^2}{\sigma_b^2}\frac{\sigma_b^2}{\sigma_c^2} = L_{S1} L_{S2} \qquad (33)$$

where $\tilde{\sigma}_b^2$ is the channel power of $\mathbf{H}_b$, the first equality is used for calculating L_S, and the second equality decomposes it into two component losses. Using our theoretical prototype model, we get $L_S = 0.58$, $L_{S1} = 0.35$, and $L_{S2} = 1.64$. We note that $L_{S1} < 1$ but $L_{S2} > 1$ reflecting the increase in channel power in beamspace versus aperture space due to broadside DLA design.

In order to calculate L_P, we can construct a $n_{full} \times n_T$ ($n_{full} \times n$) matrix $\mathbf{H}_{full}$, using the array steering vectors, representing the channel between the critically sampled transmit aperture and a critically sampled *hemisphere* (which includes the receiver aperture) located at a distance R from the center

of the transmit aperture. Using this, L_P for a particular mode (a particular feed excitation) represented by aperture domain signal $\mathbf{u}$ can be calculated as

$$L_P = L_P(\mathbf{u}) = \frac{\|\mathbf{H}_{ap}\mathbf{u}\|^2}{\|\mathbf{H}_{full}\mathbf{u}\|^2} \tag{34}$$

where $\mathbf{H}_{ap}$ is an $n_R \times n_T$ ($n \times n$) sub-matrix of $\mathbf{H}_{full}$ corresponding to the hemisphere sample points that fall within the angular extent of receive aperture (nearly identical to the aperture domain matrix $\mathbf{H}$ except for a slight difference in curvature). To determine L_P for a particular type of feed antenna, $\mathbf{u}$ is calculated using the modified columns of $\mathbf{U}_{fa}$ discussed in Sec. III-D. When the receiver is not parallel to the transmitter, $\mathbf{H}_{ap}$ still corresponds to those hemisphere sample points that fall within the angular extent of the receiver aperture, however it no longer is nearly identical to $\mathbf{H}$.

L_D can be calculated similarly to L_P by using the radiation patterns of the chosen feed antenna. Since the focal length of the designed DLA is sufficiently large compared to the size of the feed antenna (dipole or waveguide), well-known far-field radiation patterns [13] can be used. Specifically, L_D is calculated by integrating the radiation intensity pattern over the angular extent of the DLA aperture (as determined by the feed location, focal length, and aperture size), and normalizing it by the integral of the radiation intensity pattern over a full sphere. This also relates to the discussion of modifying the columns of $\mathbf{U}_{fa}$ in Sec. III-D. Normalizing each column's power to the value of L_D corresponding to the feed location and type, rather than unit power, allows the system model to directly account for L_D.

s.

REFERENCES

[1] L. Fernandes, "Developing a System Concept and Technologies for Mobile Broadband Communications," *Personal Communications, IEEE*, vol. 2, no. 1, pp. 54 –59, Feb 1995.

[2] Z. Pi and F. Khan, "An Introduction to Millimeter-Wave Mobile Broadband Systems," *Communications Magazine, IEEE*, vol. 49, no. 6, pp. 101 –107, June 2011.

[3] I. E. Telatar, "Capacity of Multi-Antenna Gaussian Channels," *European Transactions on Telecommunications*, vol. 10, pp. 585–595, 1999.

[4] D. Tse and P. Viswanath, *Fundamentals of Wireless Communication*. Cambridge University Press, 2005.

[5] A. Sayeed, "Deconstructing multiantenna fading channels," *Signal Processing, IEEE Transactions on*, vol. 50, no. 10, pp. 2563 – 2579, Oct. 2002.

[6] E. Torkildson, B. Ananthasubramaniam, U. Madhow and M. Rodwell, "Millimeter-wave MIMO: Wireless Links at Optical Speeds," in *Proc. of 44th Allerton Conference on Communication, Control and Computing*, Sept. 2006.

[7] F. Bohagen, P. Orten, and G. Oien, "Construction and capacity analysis of high-rank line-of-sight MIMO channels," in *Wireless Communications and Networking Conference, 2005 IEEE*, vol. 1, Mar. 2005, pp. 432 – 437 Vol. 1.

[8] I. Sarris and A. Nix, "Maximum MIMO Capacity in Line-of-Sight," in *Information, Communications and Signal Processing, 2005 Fifth International Conference on*, Dec. 2005, pp. 1236 –1240.

[9] A. Sayeed and N. Behdad, "Continuous Aperture Phased MIMO: Basic Theory and Applications," in *Communication, Control, and Computing (Allerton), 2010 48th Annual Allerton Conference on*, Sept. 29-Oct. 1 2010, pp. 1196 –1203.

[10] ——, "Continuous Aperture Phased MIMO: A New Architecture for Optimum Line-of-Sight Links," in *Antennas and Propagation (APSURSI), 2011 IEEE International Symposium on*, July 2011, pp. 293 –296.

[11] R. J. Mailloux, *Phased Array Antenna Handbook*, 2nd ed. Artech House, 2005.

[12] T. Deckert and A. Sayeed, "A continuous representation of multi-antenna fading channels and implications for capacity scaling and optimum array design," in *Global Telecommunications Conference, 2003. GLOBECOM '03. IEEE*, vol. 4, Dec. 2003, pp. 1786 – 1790 vol.4.

[13] C. A. Balanis, *Antenna Theory: Analysis and Design*. Wiley-Interscience, 2005.

[14] D. A. B. Miller, "Communicating with waves between volumes: Evaluating orthogonal spatial channels and limits on coupling strengths," *Appl. Opt.*, vol. 39, no. 11, pp. 1681–1699, Apr. 2000. [Online]. Available: http://ao.osa.org/abstract.cfm?URI=ao-39-11-1681

[15] E. Torkildson, H. Zhang, and U. Madhow, "Channel modeling for millimeter wave MIMO," in *Information Theory and Applications Workshop (ITA), 2010*, 31 2010-feb. 5 2010, pp. 1 –8.

[16] W. Rotman and R. Turner, "Wide-angle microwave lens for line source applications," *Antennas and Propagation, IEEE Transactions on*, vol. 11, no. 6, pp. 623 – 632, Nov. 1963.

[17] D. T. McGrath, "Planar three-dimensional constrained lenses," *IEEE Trans. Antennas Propag.*, vol. 34, no. 1, pp. 46–50, Jan. 1986.

[18] Z. Popovic and A. Mortazawi, "Quasi-optical transmit/receive front ends," *IEEE Trans. Microwave Theory Techn.*, vol. 48, pp. 1964–1975, Nov. 1998.

[19] H. Kaouach, L. Dussopt, J. Lanteri, T. Koleck, and R. Sauleau, "Circularly-Polarized discrete lens antennas in the 60-GHz band," in *ICECom, 2010 Conference Proceedings*, Sept. 2010, pp. 1 –4.

[20] A. Abbaspour-Tamijani, K. Sarabandi, and G. Rebeiz, "A millimetre-wave bandpass filter-lens array," *Microwaves, Antennas Propagation, IET*, vol. 1, no. 2, pp. 388 –395, April 2007.

[21] C. R. White, J. P. Ebling, and G. M. Rebeiz, "A wide-scan printed planar k-band microwave lens," in *Proceedings of the IEEE Antennas and Propagation International Symposium*, vol. 4A, Washington, DC, July 2005, pp. 313–316.

[22] J. Lau and S. Hum, "A Planar Reconfigurable Aperture With Lens and Reflectarray Modes of Operation," *Microwave Theory and Techniques, IEEE Transactions on*, vol. 58, no. 12, pp. 3547 –3555, Dec. 2010.

[23] M. Al-Joumayly and N. Behdad, "Wideband Planar Microwave Lenses Using Sub-Wavelength Spatial Phase Shifters," *Antennas and Propagation, IEEE Transactions on*, vol. 59, no. 12, pp. 4542 –4552, Dec. 2011.

[24] J. Butler and R. Lowe, "Beam-forming matrix simplifies design of electronically scanned antennas," *Electronic Design*, vol. 9, pp. 170–173, Apr. 1961.

[25] J. Neron and G. Delisle, "Microstrip EHF Butler Matrix Design and Realization," *ETRI Journal*, vol. 27, no. 6, Dec. 2005.

[26] T.-Y. Chin, J.-C. Wu, S.-F. Chang, and C.-C. Chang, "A V-Band 8×8 CMOS Butler Matrix MMIC," *Microwave Theory and Techniques, IEEE Transactions on*, vol. 58, no. 12, pp. 3538 –3546, dec. 2010.

[27] T. Cover and J. Thomas, *Elements of Information Theory*, ser. Wiley Series in Telecommunications and Signal Processing. Wiley-Interscience, 2006.

[28] N. Moraitis and P. Constantinou, "Indoor channel measurements and characterization at 60 ghz for wireless local area network applications," *Antennas and Propagation, IEEE Transactions on*, vol. 52, no. 12, pp. 3180 – 3189, Dec. 2004.

[29] Z. Muhi-Eldeen, L. Ivrissimtzis, and M. Al-Nuaimi, "Modelling and measurements of millimetre wavelength propagation in urban environments," *Microwaves, Antennas Propagation, IET*, vol. 4, no. 9, pp. 1300 –1309, Sept. 2010.

[30] T. Svantesson and A. Ranheim, "Mutual coupling effects on the capacity of multielement antenna systems," in *Acoustics, Speech, and Signal Processing, 2001. Proceedings. (ICASSP '01). 2001 IEEE International Conference on*, vol. 4, 2001, pp. 2485 –2488 vol.4.

[31] P. Fletcher, M. Dean, and A. Nix, "Mutual coupling in multi-element array antennas and its influence on MIMO channel capacity," *Electronics Letters*, vol. 39, no. 4, pp. 342 – 344, Feb. 2003.

[32] R. Janaswamy, "Effect of element mutual coupling on the capacity of fixed length linear arrays," *Antennas and Wireless Propagation Letters, IEEE*, vol. 1, no. 1, pp. 157 –160, 2002.

[33] J. Wallace and M. Jensen, "Mutual coupling in MIMO wireless systems: a rigorous network theory analysis," *Wireless Communications, IEEE Transactions on*, vol. 3, no. 4, pp. 1317 – 1325, July 2004.

[34] H. Friis, "A note on a simple transmission formula," *Proceedings of the IRE*, vol. 34, no. 5, pp. 254 – 256, May 1946.